

AD-A049 678

CALIFORNIA UNIV LOS ANGELES DEPT OF MATERIALS

F/G 20/11

STRESS CONCENTRATION DUE TO AN OBLATE SPHEROIDAL INCLUSION.(U)

DEC 77 M SHIBATA, K ONO

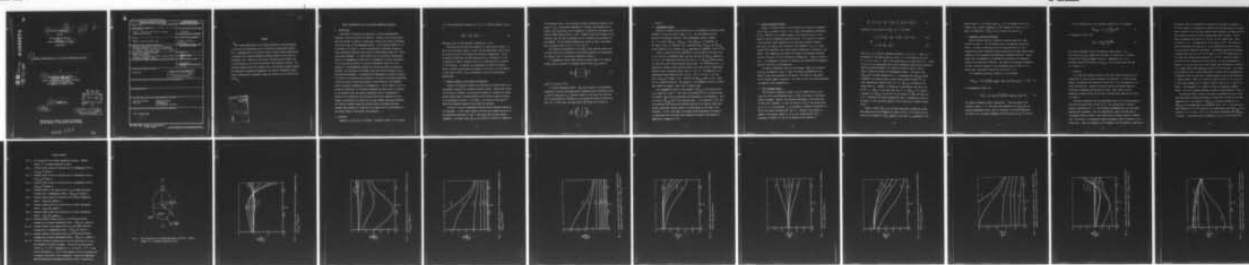
N00014-75-C-0889

UNCLASSIFIED

TR-5

NL

1 OF 1
AD
A049678



END
DATE
FILMED

2-78

DDC

AD A 049678

AD No. 700 FILE COPY

9 Technical Report No. 5
14 LTR-
to the

Office of Naval Research
15 Contract No. N00014-75-C-0889
NR 031-781

6 STRESS CONCENTRATION DUE TO AN OBLATE SPHEROIDAL INCLUSION.

by
10 Mamoru/Shibata and Kanji/Ono
MATERIALS DEPARTMENT
School of Engineering and Applied Science
University of California
Los Angeles, California 90024

11 December 1977
12 27p.

DDC
RECEIVED
FEB 7 1978
A

DISTRIBUTION STATEMENT A
Approved for public release
Distribution Unlimited

Reproduction in whole or in part is permitted
for any purpose of the United States Government

406 237

LB

REPORT DOCUMENTATION PAGE		READ INSTRUCTIONS BEFORE COMPLETING FORM
1. REPORT NUMBER ONR Technical Report # 5	2. GOVT ACCESSION NO.	3. RECIPIENT'S CATALOG NUMBER
4. TITLE (and Subtitle) Stress Concentration Due to an Oblate Spheroidal Inclusion		5. TYPE OF REPORT & PERIOD COVERED Technical
		6. PERFORMING ORG. REPORT NUMBER
7. AUTHOR(s) Mamoru Shibata and Kanji Ono		8. CONTRACT OR GRANT NUMBER(s) N00014-75-C-0889 NR 031-871
9. PERFORMING ORGANIZATION NAME AND ADDRESS Materials Department, School of Engineering 6531-Boelter Hall, University of California Los Angeles, California 90024		10. PROGRAM ELEMENT, PROJECT, TASK AREA & WORK UNIT NUMBERS
11. CONTROLLING OFFICE NAME AND ADDRESS Metallurgy Program Office of Naval Research, 800 N. Quincy Street Arlington, Virginia 22217		12. REPORT DATE December 1977
		13. NUMBER OF PAGES 25
14. MONITORING AGENCY NAME & ADDRESS (if different from Controlling Office)		15. SECURITY CLASS. (of this report) unclassified
		15a. DECLASSIFICATION/DOWNGRADING SCHEDULE
16. DISTRIBUTION STATEMENT (of this Report) Unlimited		
<div style="border: 1px solid black; padding: 5px; text-align: center;"> DISTRIBUTION STATEMENT A Approved for public release; Distribution Unlimited </div>		
17. DISTRIBUTION STATEMENT (of the abstract entered in Block 20, if different from Report)		
18. SUPPLEMENTARY NOTES		
19. KEY WORDS (Continue on reverse side if necessary and identify by block number) Internal Stresses Elasticity Theory Inclusion Inhomogeneity Non-Deformable Particle		
20. ABSTRACT (Continue on reverse side if necessary and identify by block number) See Following Page <i>over</i>		

SUMMARY

The stress concentration of an oblate spheroidal inclusion parallel to the stress and deformation axis is obtained by using Eshelby theory. This is complementary to our previous study, in which stress concentration is analyzed for an oblate spheroidal inclusion normal to the stress and deformation axis. Effects of the elastic stiffness and the aspect ratio of the inclusion on the stress concentration are examined in detail. The internal stresses inside the inclusion and at the matrix-inclusion boundary are calculated considering inhomogeneity and plastic deformation effects. Stress concentrations at graphite flakes and nodules in cast iron are discussed.

ACCESSION FOR	
NTIS	White Section <input checked="" type="checkbox"/>
DDC	Ref Section <input type="checkbox"/>
UNANNOUNCED	<input type="checkbox"/>
JUSTIFICATION	
BY	
DISTRIBUTION/AVAILABILITY CODES	
ORIG.	AVAIL. NO. OF SPECIAL
A	

STRESS CONCENTRATION DUE TO AN OBLATE SPHEROIDAL INCLUSION

1. INTRODUCTION

A good deal of attention has been given to stress concentrations produced by holes and cavities in materials. However, only limited efforts have been devoted to effects of inclusions, inside which elastic stiffnesses differ from those of the surrounding matrix. In our previous paper [1] (to be referred to as Paper I), stress concentrations in materials bearing an oblate spheroidal inclusion were studied by using Eshelby theory [2]. Three cases were considered: (1) misfit effect due to an isotropic dilatational strain; (2) inhomogeneity effect due to a difference in elastic stiffnesses of the inclusion and matrix; (3) plastic deformation effect due to the presence of a non-deformable inclusion in the matrix, which is plastically deformed. The influences of the aspect ratio and elastic stiffness of the inclusion were evaluated. In analyzing the inhomogeneity and plastic deformation effects, we restricted our attention to the case of the oblate spheroidal inclusion having its broad faces normal to the direction of the external stress and plastic deformation (N configuration). In this paper, we wish to extend our calculation to the oblate spheroidal inclusion, which is parallel to the external stress and plastic deformation axis (P configuration). Results of the calculation for the misfit effect were unaffected by this change in orientation, but those for two other effects were quite different. The internal stresses inside the inclusion and at the matrix-inclusion boundary were obtained as a function of the aspect ratio and differences in the elastic moduli of the matrix and inclusion.

2. INCLUSION

Suppose X_1 , X_2 and X_3 be a Cartesian coordinate system. At its origin

is an oblate spheroidal inclusion (cf. Fig. 1), of which boundary is given as

$$x_1^2/a^2 + (x_2^2 + x_3^2)/c^2 = 1. \quad (1)$$

The aspect ratio of the inclusion is defined by $k = a/c$.

The matrix and inclusion are assumed to be elastically isotropic. E and E^* are the Young's moduli, μ and μ^* are the shear moduli, and ν and ν^* are Poisson's ratios of the matrix and inclusion, respectively. In the following calculations, the shear modulus ratio, m , defined by $m = \mu^*/\mu$, is employed in order to describe effects of a differing elastic constant of the inclusion. To simplify the presentation of results, Poisson's ratios of matrix and inclusion are assumed to be equal to $1/3$, for which m is also equal to E^*/E . This is reasonable for most of the practical applications.

3. INTERNAL STRESSES IN AND AROUND THE INCLUSION

Eshelby [2] developed a method for obtaining the internal stress of an ellipsoidal inclusion in an infinite isotropic matrix. Eigen strain inside the inclusion is uniform. He also gave an equation to evaluate the inhomogeneity effect under a uniform external stress field by using the concept of an equivalent inclusion. As in Paper I, his theory is used here to obtain the internal stresses in and around the inclusion.

In Paper I, only two independent principal stress components needed to be considered. In this study, however, all three are required since one of the geometrical symmetries is lost. This change adds one more unknown component of the eigen strain e_{ij}^T of the equivalent inclusion in comparison

to the previous study. After solving the proper simultaneous equations with respect to e_{ij}^T , the principal components of internal stress within the inclusion, σ_{11}^I , σ_{22}^I and σ_{33}^I , can be obtained as a function of the aspect ratio k and the shear modulus ratio $m = \mu^*/\mu$. Internal stress just outside of the inclusion, σ_{ij}^M , can also be obtained, but is a function of the position at the boundary. We will present primarily the results of σ_{11}^M at the equator point A_3 along X_3 axis or $(0, 0, c)$ (cf. Fig. 1).

Two effects are considered in this study, since internal stresses due to misfit effect can be obtained for the present geometry by interchanging the indices 1 and 3 in the results presented in Paper I:

1) Inhomogeneity effect: When uniaxial external stress σ^A is applied along X_3 axis at infinity, it produces elastic strain, e_{ij}^A , given by

$$e_{ij}^A = \begin{pmatrix} -\nu & 0 & 0 \\ 0 & -\nu & 0 \\ 0 & 0 & 1 \end{pmatrix} e^A \quad (2)$$

where e^A is equal to σ^A/E .

2) Plastic deformation effect: When the inclusion is non-deformable plastically, and the surrounding matrix undergoes plastic deformation along X_3 axis by the amount of ϵ_p , internal stresses in and around the inclusion are to be evaluated as a function of ϵ_p following the method of Tanaka and Mori [3]. In this case, the eigen strain e_{ij}^{T*} inside the inclusion is

$$e_{ij}^{T*} = \begin{pmatrix} \frac{1}{2} & 0 & 0 \\ 0 & \frac{1}{2} & 0 \\ 0 & 0 & -1 \end{pmatrix} \cdot \epsilon_p$$

4. RESULTS

4.1 Inhomogeneity Effect

Results of internal stress evaluation due to inhomogeneity effect for seven different m values are shown in Figs. 2 to 4. All the stresses are normalized by the applied stress σ^A . When inhomogeneity effect is absent ($m = 1$), we have $(\sigma_{11}^I)_{inh} = (\sigma_{22}^I)_{inh} = 0$ and $(\sigma_{33}^I)_{inh} = \sigma^A$ regardless of the aspect ratio k , as expected. As k approaches zero, $(\sigma_{11}^I)_{inh}$ and $(\sigma_{22}^I)_{inh}$ vanish regardless of m , whereas $(\sigma_{33}^I)_{inh}$ approaches an asymptotic values of $m\sigma^A$.

Figure 2 indicates that the magnitude of stress normal to the broad face of the inclusion is generally small, and that the sign of $(\sigma_{11}^I)_{inh}$ changes at $k \approx 0.37$. For elastically hard inclusion with $m > 1$, $(\sigma_{11}^I)_{inh}$ becomes tensile for thin discs under tensile loading along X_3 axis. For inclusions, with $m > 1$, compressive (tensile) stress develops along X_2 axis when tensile (compressive) external stress is applied along X_3 axis (cf. Fig. 3). The magnitude of the compressive stress depends on both k and m . For $k = 0.07$ and $m = 10$, the ratio $(\sigma_{22}^I)_{inh}/\sigma^A$ reaches -0.473 . Results for $(\sigma_{33}^I)_{inh}$ shown in Fig. 4 indicate no unexpected behavior. The approach to the asymptotic value is, however, much slower for larger m values than for smaller ones.

For inhomogeneity effect at the boundary, $(\sigma_{11}^M)_{inh}$ at the equator point A_3 is presented in Fig. 5. The stress (as normalized by σ^A) is positive when m is greater than unity and increases with decreasing k or increasing m . For m less unity, $(\sigma_{11}^M)_{inh}$ and σ^A have opposite signs. It is important to note that an elastically hard plate-like inclusion parallel to the tensile stress axis produce significant tensile stress at the edge normal to the plane of the inclusion. On the other hand, the tensile stress developed at the edge of an elastically soft inclusion under compressive loading is much smaller in magnitude in comparison to σ^A .

4.2 Plastic Deformation Effect

Results of internal stress in the inclusion due to plastic deformation effect $(\sigma_{ij}^I)_p$ are shown in Figs. 6 to 8. Here, the stresses are normalized by $E^*\epsilon_p$, where E^* is the Young's modulus of the inclusion and ϵ_p is the amount of plastic deformation along the X_3 axis. For a given k , a smaller m value produces larger magnitude of all principal stresses in general. Both $(\sigma_{11}^I)_p$ and $(\sigma_{22}^I)_p$ have the opposite sign compared to ϵ_p ; i.e., these stresses are compressive when tensile plastic deformation is produced in the matrix. Their magnitudes are smaller for larger m and approach asymptotic values of zero and -0.19 with vanishing k , respectively. $(\sigma_{33}^I)_p$ is shown in Fig. 8. Its magnitude is greater for smaller m and approaches the asymptotic value of $0.9375 E^*\epsilon_p$ with decreasing k .

For plastic deformation effect at the boundary, $(\sigma_{11}^M)_p$ at the equator point A_3 is presented in Fig. 9. Here, the stress is normalized by $E\epsilon_p$ where E is the Young's modulus of the matrix. The effect of the modulus ratio m becomes larger at smaller k . As k goes to zero, the stress approaches an asymptotic value depending on m .

4.3 σ_{11}^M at Equator Points

The inclusion considered in Paper I has the symmetry about X_3 axis (also the stress and deformation axis), so σ_{33}^M at any point on the equator remains unchanged. However, the inclusion considered in this study does not have such a symmetry. So far, the results of σ_{11}^M at the equator point A_3 or $(0, 0, c)$ are presented. It is necessary to examine the variation of σ_{11}^M on the equator defined by $X_2^2 + X_3^2 = c^2$. Consider a unit vector, \bar{n} , normal to the equator, where $\bar{n} = (0, n_2, n_3)$, satisfying $n_2^2 + n_3^2 = 1$. According to Eshelby [2], σ_{11}^M on the equator can be obtained as

$$\sigma_{11}^M = \frac{3}{4} E \{ (e_{11}^c + e_{kk}^c) - \frac{1}{2} e_{kk}^T - \frac{1}{2} (e_{22}^T n_2^2 + e_{33}^T n_3^2) \} \quad (4)$$

Equation (4) can be written as $\sigma_{11}^M = C_1 + C_2 n_3^2$, where

$$C_1 = \frac{3}{4} E \{ (e_{11}^c + e_{kk}^c) - \frac{1}{2} (e_{11}^T + 2e_{22}^T + e_{33}^T) \} \quad (4a)$$

and

$$C_2 = \frac{3}{8} E (e_{22}^T - e_{33}^T). \quad (4b)$$

Since $0 \leq n_3 \leq 1$, σ_{11}^M has a maximum at either $n_3 = 0$ or $n_3 = 1$. Here, $n_3 = 1$ corresponds to the equator point A_3 , and $n_3 = 0$ to the equator point A_2 or $(0, c, 0)$ (cf. Fig. 1). σ_{11}^M at the equator point A_2 is then equal to C_1 . Values of σ_{11}^M at A_2 for inhomogeneity and plastic deformation effects were calculated. These are presented against k for various m values in Figs. 10 and 11.

Figure 10 shows the results for inhomogeneity effect. The stress ratio $(\sigma_{11}^M)_{inh}/\sigma^A$ is always negative for $m > 1$, indicating that $(\sigma_{11}^M)_{inh}$ reaches a maximum at the equator point A_3 under tensile applied stress ($\sigma^A > 0$). Under compressional applied stress ($\sigma^A < 0$), $(\sigma_{11}^M)_{inh}$ is maximum at the equator point A_2 . However, its magnitude is much smaller than that at A_3 for $\sigma^A > 0$. When m is less than unity and $\sigma^A > 0$, $(\sigma_{11}^M)_{inh}$ at A_2 reaches a maximum, but $(\sigma_{11}^M)_{inh}$ at any point on the equator is always less than that of σ^A . Therefore, the stress concentration due to inhomogeneity effect at the edge of a soft inclusion parallel to the stress axis is deemed insignificant.

Figure 11 shows $(\sigma_{11}^M)_p$ at A_2 arising from plastic deformation effect. When these results are compared with those in Fig. 9, it is found that the location of a maximum in $(\sigma_{11}^M)_p$ depends on the sign of ϵ_p regardless of the

modulus ratio m . For tensile strain ($\epsilon_p > 0$), the maximum occurs at A_3 , whereas $(\sigma_{11}^M)_p$ reaches a maximum at A_2 for compressive strain ($\epsilon_p < 0$). Again, the magnitude of $(\sigma_{11}^M)_p$ at A_2 is smaller than that at A_3 .

4.4 Comparison with Previous Results

Results obtained here for a spherical inclusion agree with those reported in Paper I. For this special case, no geometrical distinction exists. It should be mentioned here that Tanaka and Mori [3] first evaluated the plastic deformation effect quantitatively using Eshelby theory. Originally, they considered work-hardening of composite materials. Later, Tanaka, Mori and Nakamura [4,5] extended the calculations to decohesion process of an inclusion in material. The shape of the inclusion considered included a thin disc parallel to the deformation axis X_3 (with $k = 0$), a sphere, and a long needle along the X_3 axis (with $k = \infty$).

For a spherical inclusion, Tanaka et al. [4] obtained

$$(\sigma_{33}^I)_{inh} = \left\{ \frac{10}{(7-5\nu) + (8-10\nu)m} + \frac{1}{2(1-2\nu) + (1+\nu)m} \right\} (1-\nu) \cdot m \cdot \sigma^A \quad (5)$$

for inhomogeneity effect and

$$(\sigma_{33}^I)_p = \frac{(7-5\nu)}{(7-5\nu)(1+\nu) + (8-10\nu)(1+\nu)m} \cdot E^* \epsilon_p \quad (6)$$

for plastic deformation effect, respectively. These are given in our notation, taking $\nu = \nu^*$. Note that their expression for $(\sigma_{33}^I)_p$ has one obvious typographical error, which is corrected in the above expression.

Our results are in complete agreement with theirs given in Eqs. (5) and (6).

For an infinitely thin disc inclusion, Tanaka et al. [5] obtained

$$(\sigma_{33}^I)_{inh} = \left\{ 1 + \frac{2\nu^3}{(1 - \nu^2)^2} \right\} m\sigma^A \quad (7)$$

or inhomogeneity effect and

$$(\sigma_{33}^I)_P = \frac{(2 - \nu + \nu^2)E^*\epsilon_P}{2(1 - \nu^2)} \quad (8)$$

for plastic deformation effect, respectively, again taking $\nu = \nu^*$.

Their result for $(\sigma_{33}^I)_P$ agrees with ours when ν is taken as 1/3. However, the result for $(\sigma_{33}^I)_{inh}$ disagrees with ours. Apparently, Eq. (7) is erroneous because the equality of $(\sigma_{33}^I)_{inh} = \sigma^A$ is not satisfied even when $m = 1$ unless $\nu = 0$.

5. DISCUSSION

It is known that graphite flakes in cast iron initiate fracture and are responsible for the low tensile strength of the material. In most previous studies, the graphite was treated as a cavity ($E^* = 0$) in the analysis of the stress concentration. However, the elastic modulus and thermal expansion coefficient of graphite are obviously not zero. Their effects on the mechanical strength of cast iron can now be analyzed more explicitly by using our results.

The shape of graphite flake is approximated here to be an oblate spheroid, which has the aspect ratio of 0.01 to 0.2. The limiting case of nodular graphite corresponds to $k = 1$. Two different arrangements for the disc shaped graphite were considered. One is N configuration, where the broad face of the graphite flake is normal to the stress axis of uniaxial tension or compression. The other is P configuration where the graphite flake is parallel to the stress axis. These are referred to as "N graphite" and "P graphite", respectively.

The maximum stress for decohesion of graphite-iron interface is expected to be stress normal to the graphite-iron interface at the polar point B or normal stress (parallel to the inclusion symmetry axis) acting at the equator point A. Three different effects of stress concentrations were evaluated. Young's moduli of graphite and iron are 20.7 GPa and 206 GPa, respectively. Thus, we obtain $m = 0.1$. The magnitude of σ^A was taken as $10^{-3}E$. The amount of plastic deformation was taken as 1%. It is assumed that the matrix ceases to allow plastic relaxation below 800°K. The thermal expansion coefficients of graphite and iron are $1.8 \times 10^{-6}/^{\circ}\text{K}$ and $12.0 \times 10^{-6}/^{\circ}\text{K}$, respectively [6]. This gives the thermal misfit strain of $\epsilon^T = 5 \times 10^{-3}$. Results of Paper I were used for the calculation of misfit effect. For each configuration of graphite, the total stress due to three effects was calculated as a function of k , taking tensile and compressive nature of σ^A into account. The results are presented in Fig. 12, where each curve is labeled for the configuration of graphite flake, the position of internal stress as well as the direction of applied stress. Here, (P, A) refers to σ_{11}^M at A_3 and (P, B) to σ_{11}^I at B in this study, whereas (N, A), refers to σ_{33}^M at A and (N, B) to σ_{33}^I at B in Paper I. The subscript T or C refers to tensile or compressive applied stress. Note that stresses are given in terms of Young's modulus of iron, E .

As expected, tensile stress at the edge of N graphite $(N, A)_T$ is quite high under tensile loading and fracture is expected to initiate at the edge regardless of k . For smaller k , $(\sigma_{33}^M)_{\text{mis}}$ is the main contribution, but $(\sigma_{33}^M)_{\text{inh}}$ is also significant as k approaches unity. At $k = 0.01$, the sum of three effects is $20 \times 10^{-3}E$, which is five times smaller than $(\sigma_{33}^M)_{\text{inh}}$ for a cavity ($m = 0$, $k = 0.01$). At $k = 0.1$, the sum is 40% greater than $(\sigma_{33}^M)_{\text{inh}}$ of cavity. On the broad face of N graphite, $(N, B)_T$ is still tensile for

$k < 0.45$ but its magnitude is lower than that of σ^A . Both $(N, A)_C$ and $(N, B)_C$ are mostly compressive, so N graphite is expected to be an inactive source for fracture under compressive loading.

It is most surprising that both $(P, A)_T$ and $(P, A)_C$ are positive and large in magnitude, especially for $k < 0.1$. This implies that tensile stress acts at the edge of P graphite under tensile or compressive loading. Low tensile fracture strength of gray cast iron is thus expected from misfit effect as well as from inhomogeneity effect, not merely from the latter. Some plastic deformation in the vicinity of graphite flakes is also expected because of very high stress level. This contradicts our assumption and invalidates a part of our calculations. However, general features of the results are still applicable.

Deleterious effects of graphite flakes are present even under compressive loading according to the present calculation. Still, the degree of stress concentration is much less under compression than under tension. This is the obvious origin of the strength differential effect in gray cast iron [7]. Another obvious consequence is the favorable effect of spheroidization of graphite [8], as is well known industrially. However, the stress concentration at the side of a nodular graphite is more than 50% higher than that of an equivalent cavity.

REFERENCES

1. M. Shibata and K. Ono, to be published in Acta Metallurgica.
2. J. D. Eshelby, Proc. Roy. Soc., A241 (1957) 376.
3. K. Tanaka and T. Mori, Acta Metall., 18 (1970) 931.
4. K. Tanaka, T. Mori and T. Nakamura, Phil. Mag., 21 (1970) 267.
5. K. Tanaka, T. Mori and T. Nakamura, Trans. Iron and Steel Inst. Japan, 11 (1971) 383.
6. Y. S. Touloukian (ed.), Thermophysical Properties of High Temperature Solid Materials, The Macmillan Company, New York, 1966, Vol. 1.
7. J. O. Draffin and W. L. Collins, Proc. ASTM, 39 (1939) Part 2, 589.
8. T. W. Curry, Cast Metals Handbook, Amer. Foundrymen's Soc., Illinois, 1957, p. 195.

FIGURE CAPTIONS

- Fig. 1. The orientation of an oblate spheroidal inclusion. Applied stress, σ^A , is exerted along the X_3 axis.
- Fig. 2. Internal stress inside the inclusion due to inhomogeneity effect, $(\sigma_{11}^I)_{inh}/\sigma^A$ against k .
- Fig. 3. Internal stress inside the inclusion due to inhomogeneity effect, $(\sigma_{22}^I)_{inh}/\sigma^A$ against k .
- Fig. 4. Internal stress inside the inclusion due to inhomogeneity effect, $(\sigma_{33}^I)_{inh}/\sigma^A$ against k .
- Fig. 5. Internal stress at the equator point A_3 on the matrix-inclusion boundary due to inhomogeneity effect, $(\sigma_{11}^M)_{inh}/\sigma^A$ against k .
- Fig. 6. Internal stress inside the inclusion due to plastic deformation effect, $(\sigma_{11}^I)_p/E\epsilon_p$ against k .
- Fig. 7. Internal stress inside the inclusion due to plastic deformation effect, $(\sigma_{22}^I)_p/E\epsilon_p$ against k .
- Fig. 8. Internal stress inside the inclusion due to plastic deformation effect, $(\sigma_{33}^I)_p/E\epsilon_p$ against k .
- Fig. 9. Internal stress at equator point A_3 on the matrix-inclusion boundary due to plastic deformation effect, $(\sigma_{11}^M)_p/E\epsilon_p$ against k .
- Fig. 10. Internal stress at the equator point A_2 on the matrix-inclusion boundary due to inhomogeneity effect, $(\sigma_{11}^M)_{inh}/\sigma^A$ against k .
- Fig. 11. Internal stress at the equator point A_2 on the matrix-inclusion boundary due to plastic deformation effect, $(\sigma_{11}^M)_p/E\epsilon_p$ against k .
- Fig. 12. Internal stresses at equator point A and the polar point B of iron matrix-graphite inclusion boundary. The sum of the three effects (misfit $\epsilon_p = 5 \times 10^{-3}$, inhomogeneity $m = 0.1$ with $\sigma^A = 10^{-3} \cdot E$, and plastic deformation $\epsilon_p = 1\%$) is shown against k for two configurations of graphite inclusions; N and P graphites. Tensile and compressive applied stresses are indicated by subscript T and C, respectively.

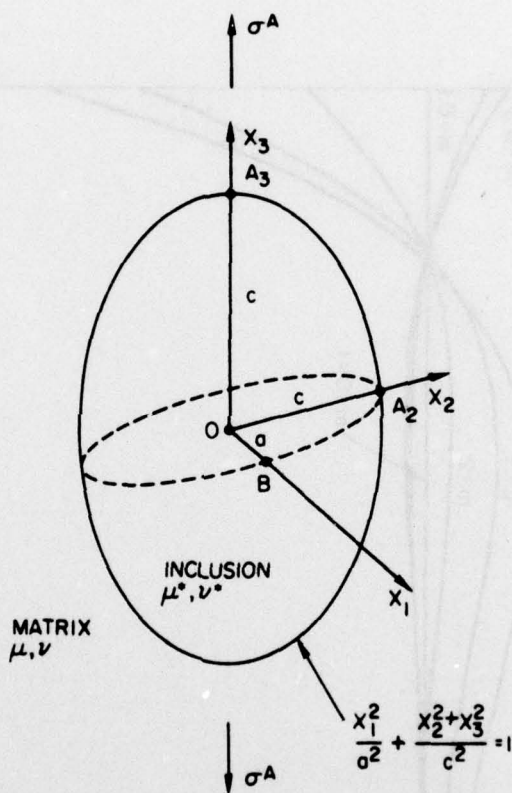


Fig. 1. The orientation of an oblate spheroidal inclusion. Applied stress, σ^A , is exerted along the x_3 axis.

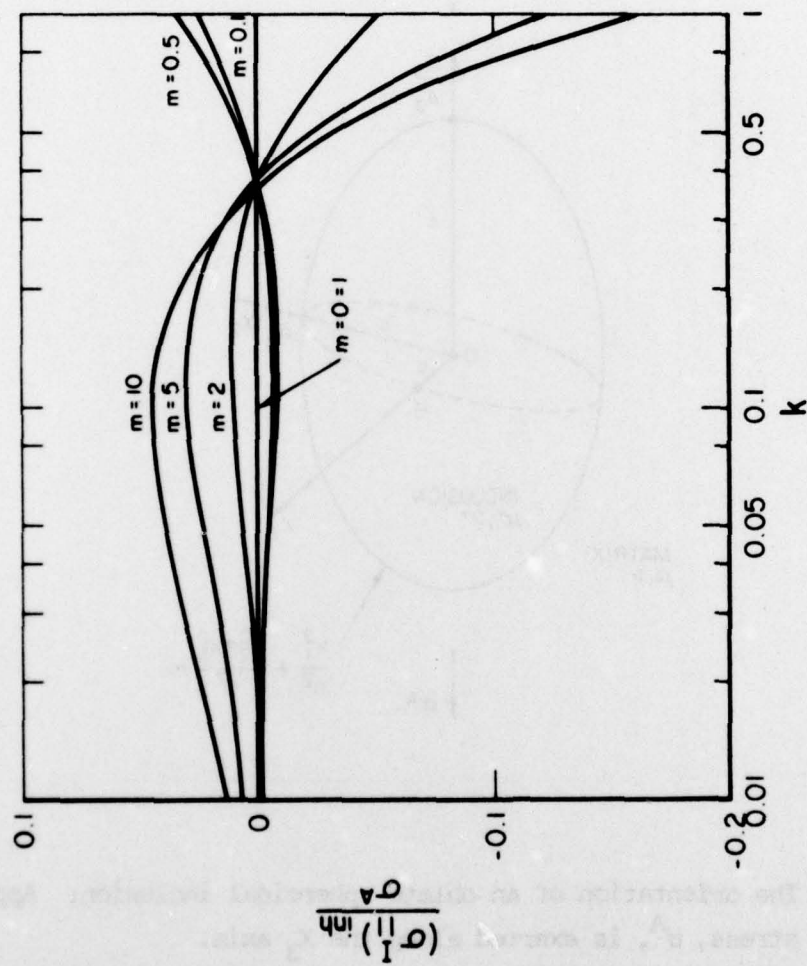


Fig. 2. Internal stress inside the inclusion due to inhomogeneity effect, $(\sigma_{II}^I)_{inh}/\sigma^A$ against k .

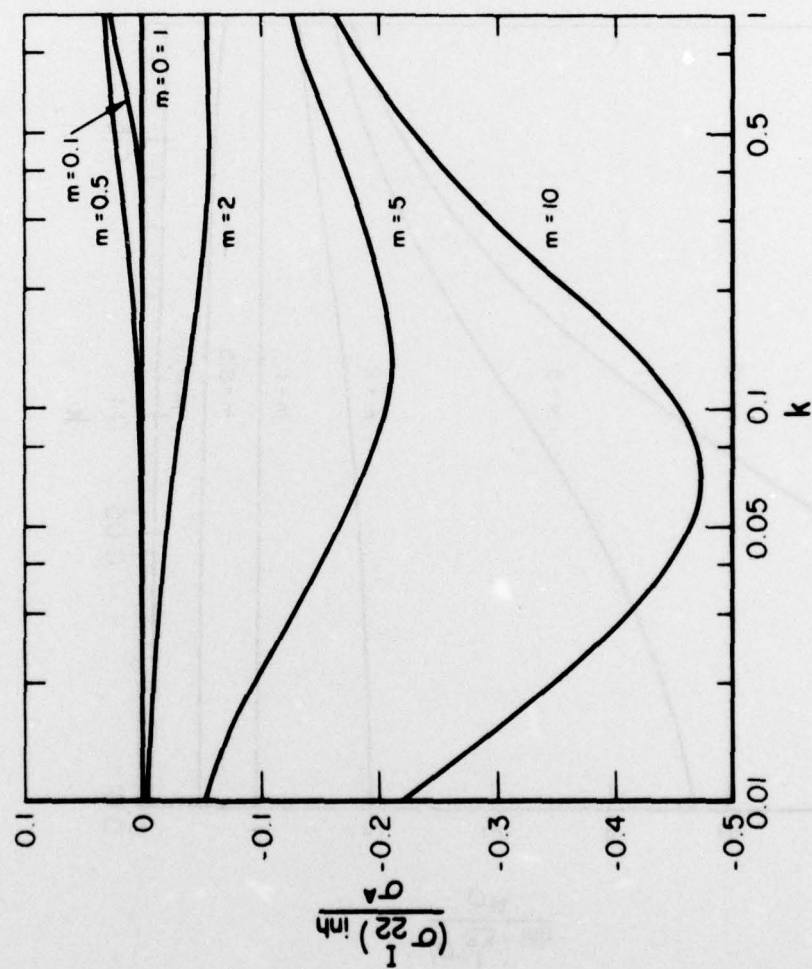


Fig. 3. Internal stress inside the inclusion due to inhomogeneity effect, $(\sigma_{22}^I)_b / \sigma^A$ against k .

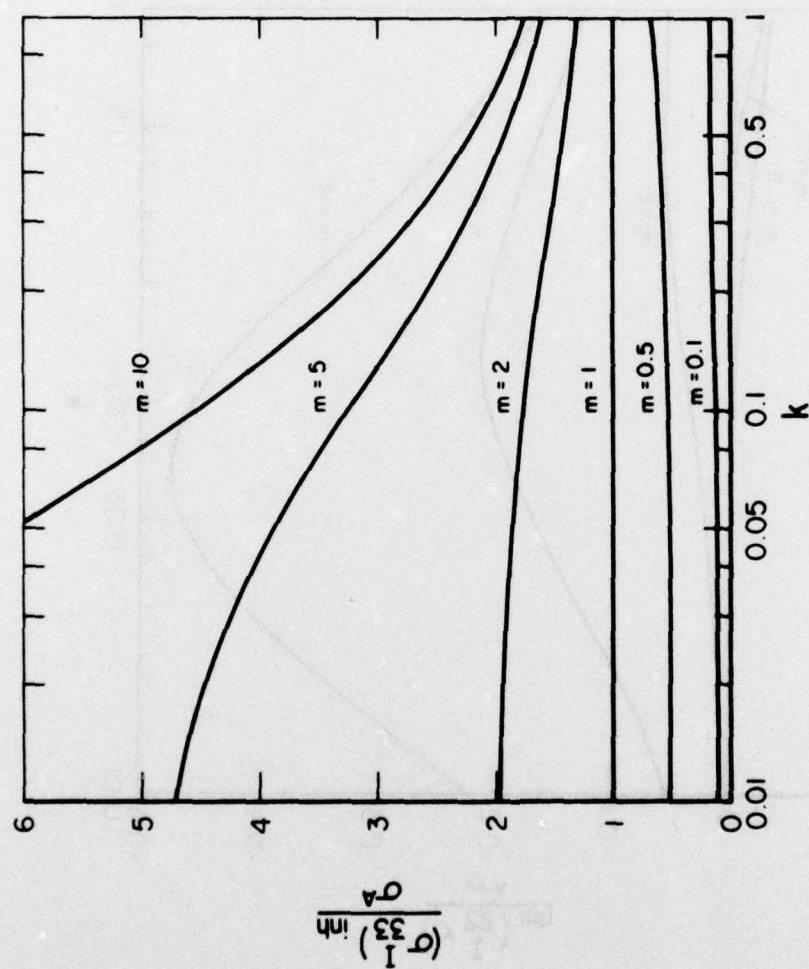


Fig. 4. Internal stress inside the inclusion due to inhomogeneity effect, $(\sigma_{33})_{inh}/\sigma^A$ against k .

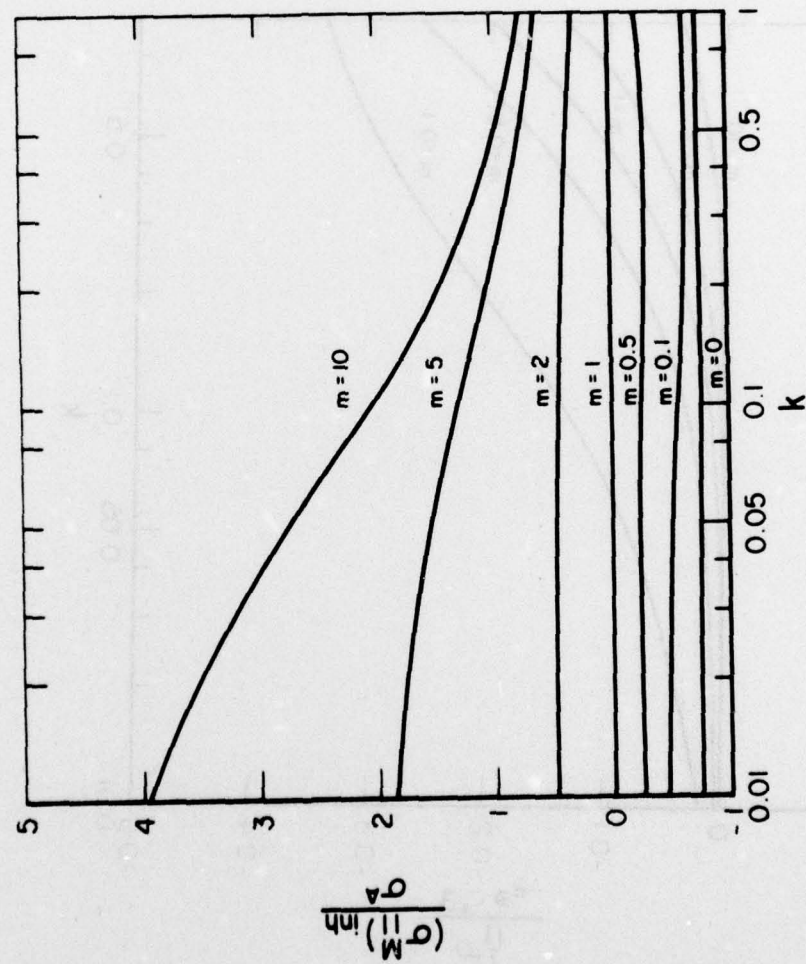


Fig. 5. Internal stress at the equator point A_3 on the matrix-inclusion boundary due to inhomogeneity effect, $(\sigma_{11}^M)_{inh}/\sigma^A$ against k .

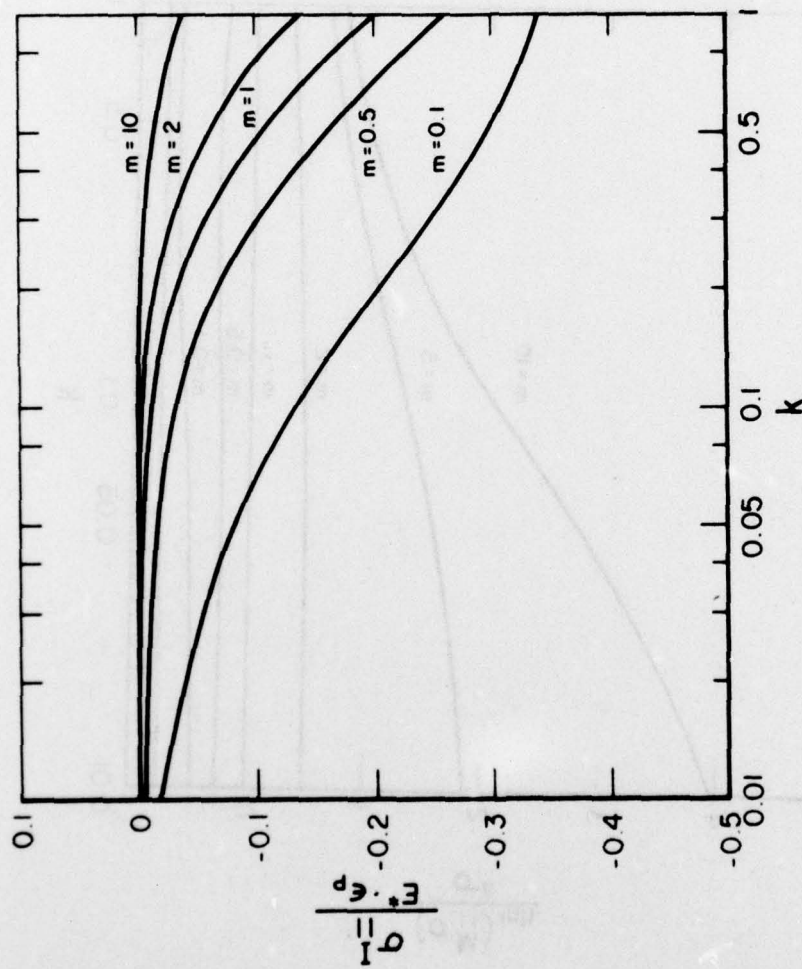


Fig. 6. Internal stress inside the inclusion due to plastic deformation effect, $(\sigma_{II}^I)_p / E^* \epsilon_p$ against k .

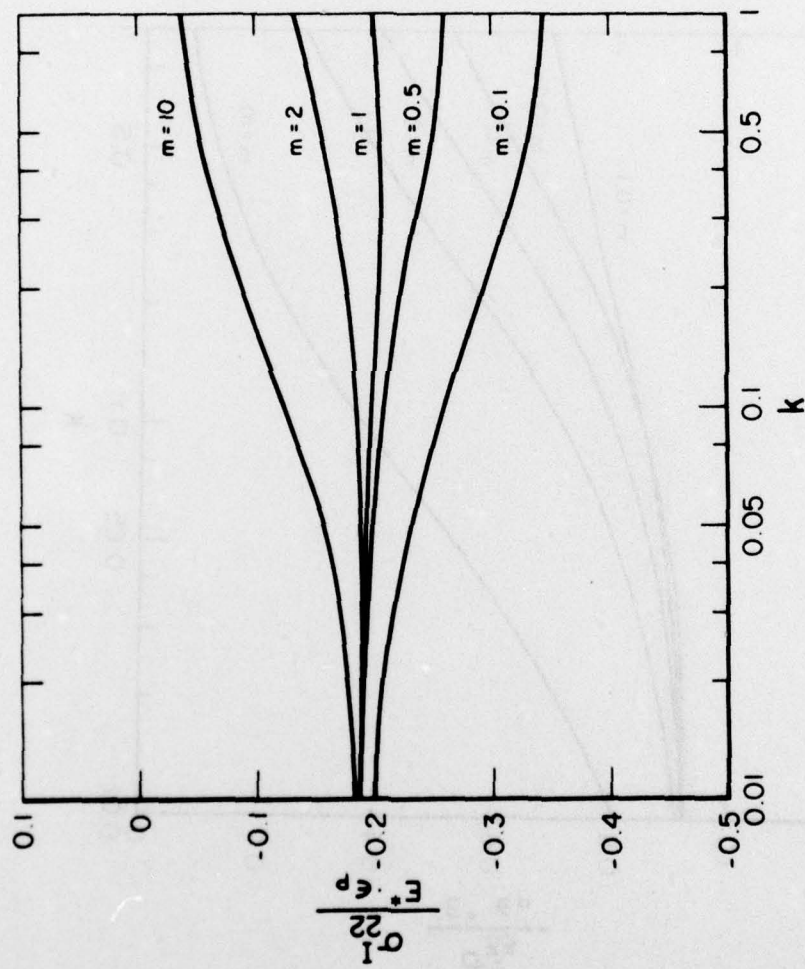


Fig. 7. Internal stress inside the inclusion due to plastic deformation effect, $(\sigma_{22}^I)/E^*\epsilon_p$ against k .

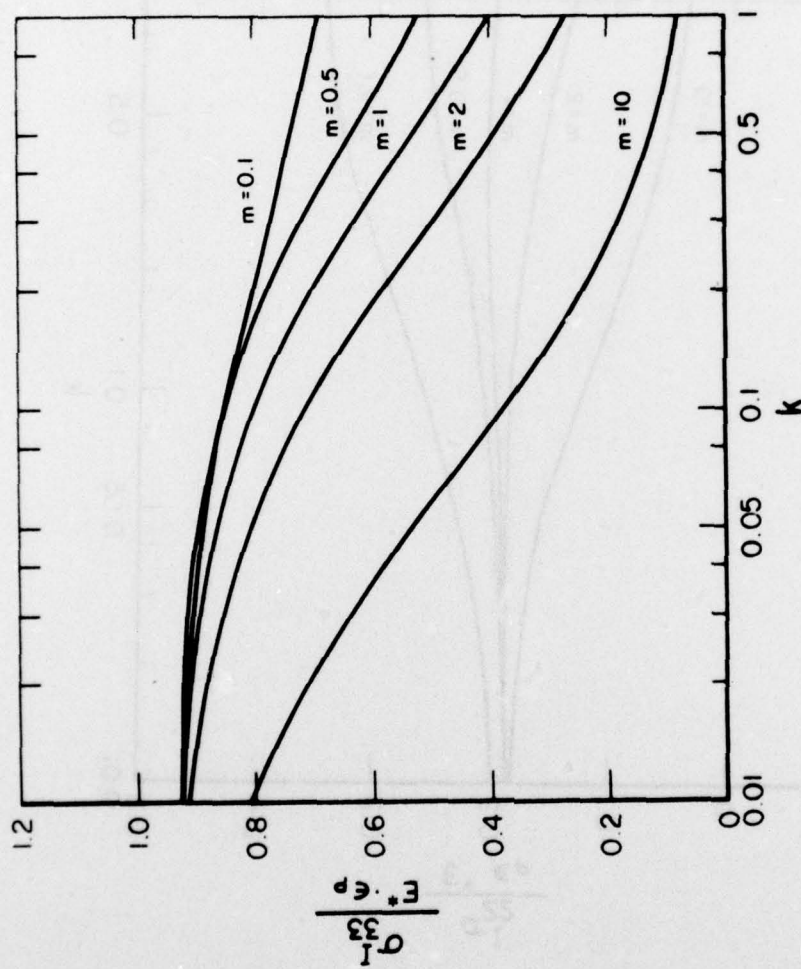


Fig. 8. Internal stress inside the inclusion due to plastic deformation effect, $(\sigma_{33})_I / E\epsilon_p$ against k .

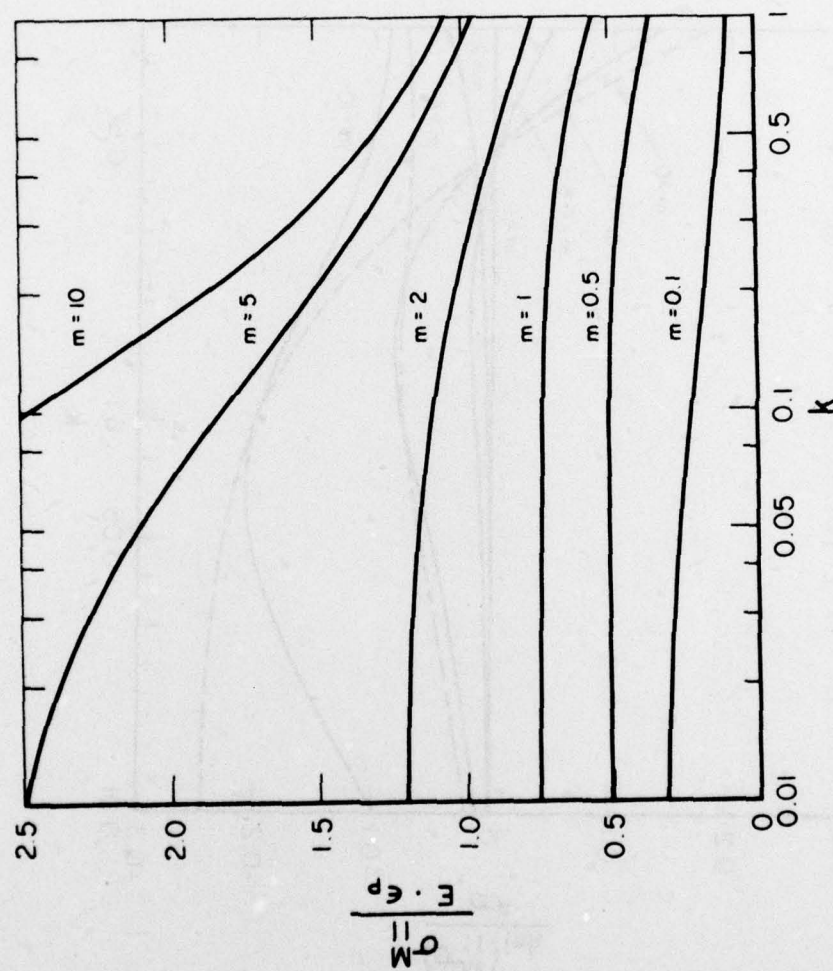


Fig. 9. Internal stress at equator point A_3 on the matrix-inclusion boundary due to plastic deformation effect, $(\sigma_{11}^M)_p / E \cdot \epsilon_p$ against k .

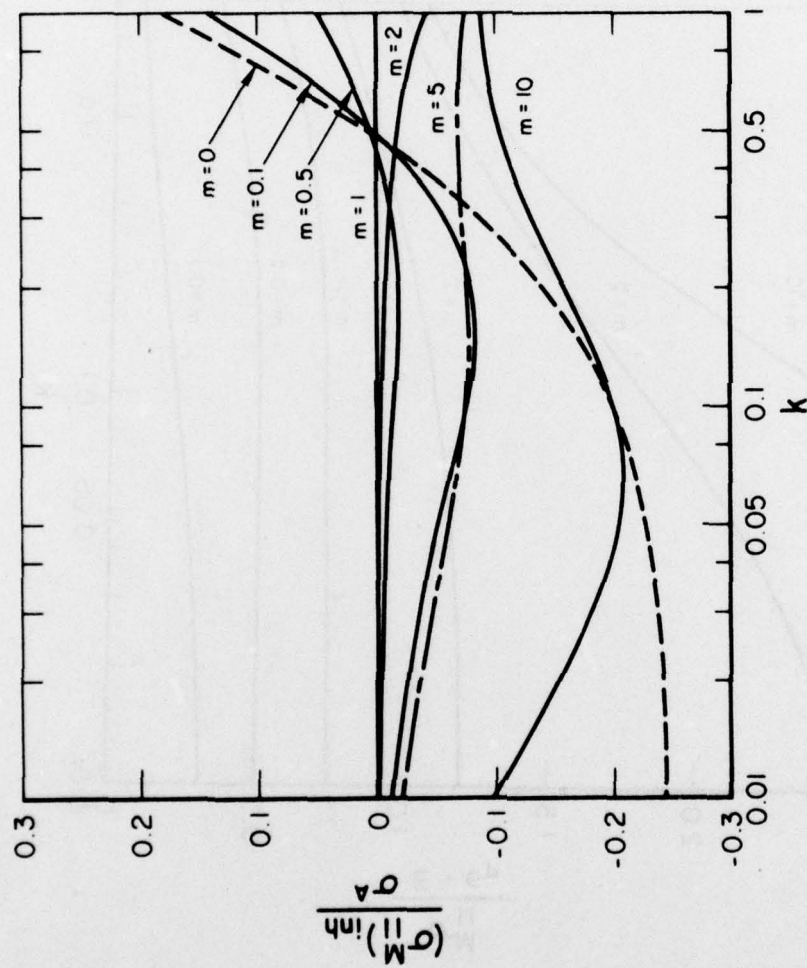


Fig. 10. Internal stress at the equator point A_2 on the matrix-inclusion boundary due to inhomogeneity effect, $(\sigma_{11})_{inh}^M / \sigma^A$ against k .

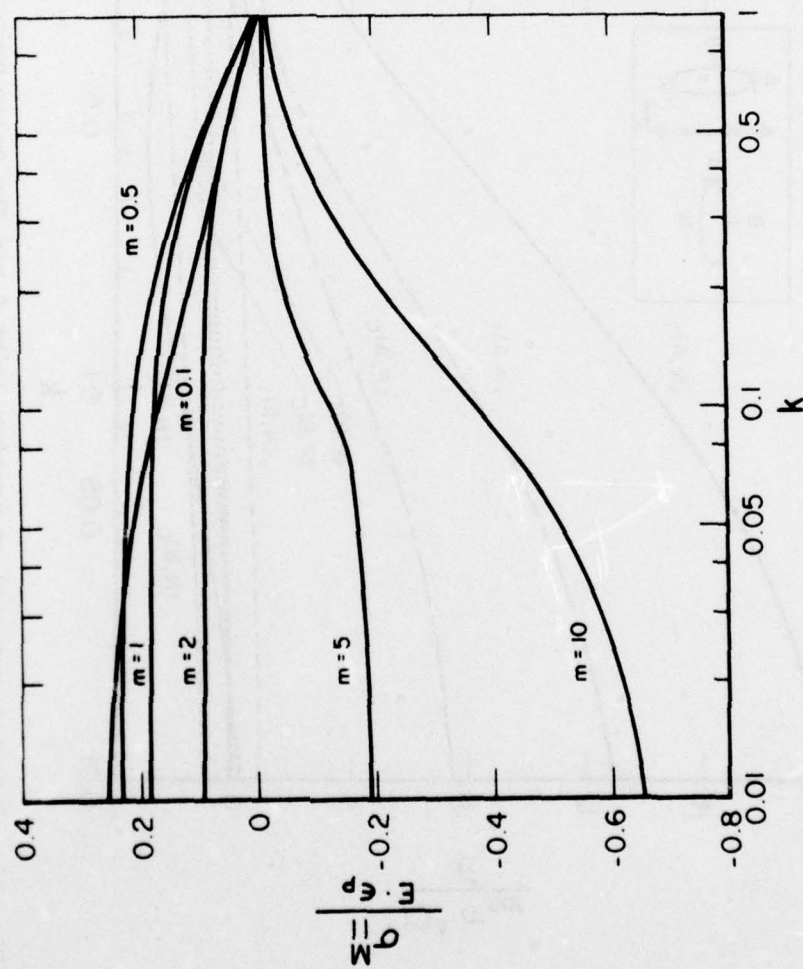


Fig. 11. Internal stress at the equator point A_2 on the matrix-inclusion boundary due to plastic deformation effect, $(\sigma_{11}^M)_p / E \cdot \epsilon_p$ against k .

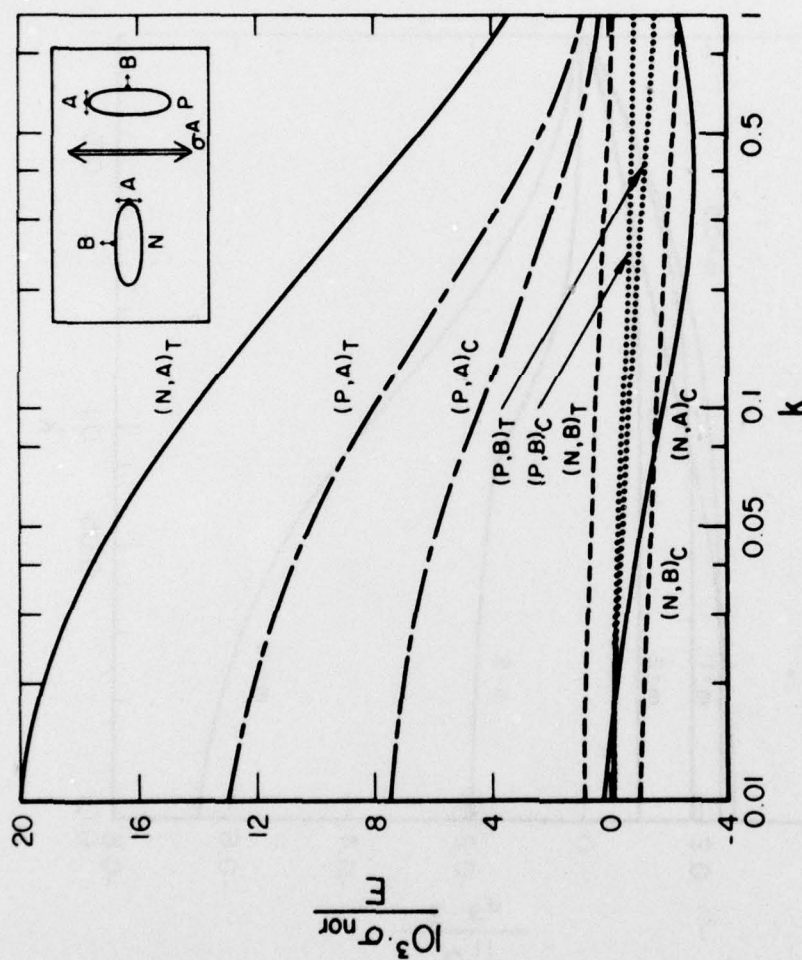


Fig. 12. Internal stresses at equator point A and the polar point B of iron matrix-graphite inclusion boundary. The sum of the three effects (misfit $\epsilon_p = 5 \times 10^{-3}$, inhomogeneity $m = 0.1$ with $\sigma^A = 10^{-3} \cdot E$, and plastic deformation $\epsilon_p = 1\%$) is shown against k for two configurations of graphite inclusions; N and P graphites.